Chakraborty, Tirthankar; Sarangi, Chandan; Krishnan, Mithun; Tripathi, Sachchida Nand; Morrison, Ross; Evans, Jonathan. 2019. **Biases in model-simulated surface energy fluxes during the Indian monsoon onset period**. *Boundary-Layer Meteorology*, 170 (2). 323-348. https://doi.org/10.1007/s10546-018-0395-x

Biases in Model-Simulated Surface Energy Fluxes During the Indian Monsoon Onset Period

Tirthankar Chakraborty · **Chandan Sarangi** · **Mithun Krishnan** · **Sachchida Nand Tripathi** · **Ross Morrison** · **Jonathan Evans**

Abstract We use eddy covariance measurements over a semi-natural grassland in the central Indo-Gangetic Basin to investigate biases in the energy fluxes simulated by the Noah land-surface model (LSM) for two monsoon onset periods: one with rain (2016) and one completely dry (2017). In the preliminary run with default parameters, the offline Noah LSM overestimates the midday (1000 to 1400 local time) sensible heat flux (H) by 279% (in 2016) and 108% (in 2017) and underestimates the midday latent heat flux (LE) by 56% (in 2016) and 67% (in 2017). These discrepancies in simulated energy fluxes propagate to and are amplified in coupled Weather Research and Forecasting (WRF) model simulations, as seen from the High Asia Reanalysis (HAR) dataset. One-dimensional Noah simulations with modified site-specific vegetation parameters not only improve the partitioning of the energy fluxes (Bowen ratio of 0.90 in modified run versus 3.09 in the default run), but also

Tirthankar Chakraborty
Centre for Environmental Science & Engineering, IIT Kanpur, India and School of Forestry & Environmental Studies, Yale University, CT, USA
E-mail: tirthankar25@gmail.com

Chandan Sarangi
Civil Engineering Department, IIT Kanpur, India and Pacific Northwest National Laboratory, WA, USA USA
E-mail: chandansarangi591@gmail.com

Mithun Krishnan
Environmental Engineering and Management Programme, IIT Kanpur, India
E-mail: mithunkv@iitk.ac.in

Sachchida Nand Tripathi (corresponding author)
Civil Engineering Department and Centre for Environmental Science & Engineering, IIT Kanpur, India
E-mail: snt@iitk.ac.in

Ross Morrison
Centre for Ecology & Hydrology, Wallingford, UK
E-mail: rosrri@ceh.ac.uk

Jonathan Evans
Centre for Ecology & Hydrology, Wallingford, UK
E-mail: jge@ceh.ac.uk

reduce the overestimation of the model-simulated soil and skin temperature. Thus, use of ambient site parameters in future studies is warranted to reduce uncertainties in short-term and long-term simulations over this region. Finally, we examine how biases in the model simulations can be attributed to lack of closure in the measured surface energy budget. The bias is smallest when the sensible heat flux post-closure method is used (5.2 W m^{-2} for H and 16 W m^{-2} for LE in 2016; 0.17 W m^{-2} for H and 2.8 W m^{-2} for LE in 2017). The study shows the importance of taking into account the surface energy imbalance at eddy covariance sites when evaluating LSMs.

Keywords Eddy covariance · Energy balance closure · Land-surface model · Model evaluation · Surface energy balance

1 Introduction

The Earth is a complex system and its principal components, the atmosphere, the ocean, and the land, interact with each other on a wide range of spatial and temporal scales (Suni et al. 2015). The impact of land-atmosphere interactions on climatic variabilities has received much attention in recent years (Seneviratne and Stöckli 2008). The land surface represents the lower boundary for the atmosphere and interacts with it through the exchange of energy, water, and a variety of chemical species (Entekhabi et al. 1999). Solar radiation warms the Earth's surface, and the total available energy is primarily partitioned into sensible heat flux (henceforth, H), latent heat flux (henceforth, LE), and ground heat flux (henceforth, G_s), collectively representing the surface energy balance (Trenberth et al. 2009). Studies have shown that the heterogeneity of the Earth's land surface makes the feedbacks between land use and the energy fluxes dynamic in space and time (Giorgi and Avissar 1997; Pielke 2001; Suni et al. 2015). Thus, forecasting both climate and weather requires proper incorporation of these feedbacks in model formulations.

An increasing body of evidence demonstrates that land-surface models (LSMs) show large uncertainties when simulating the partitioning between the energy fluxes (Abramowitz et al. 2007; Jiménez et al. 2011; Haughton et al. 2016; Ukkola et al. 2016). Of particular note is the recent Protocol for the Analysis of Land Surface models (PALS) Land sUrface Model Benchmarking Evaluation pRoject (PLUMBER) on the evaluation of 13 LSMs, which revealed that all LSMs were outperformed by simple, regression-based empirical models (Haughton et al. 2016). Another recent study found that LSMs systematically underestimate LE during drought conditions (Ukkola et al. 2016). In addition to the modelling uncertainties, the measured surface energy balance is almost never closed, with the sum of observed H, LE and G_s consistently showing a lower magnitude than the observed net radiation (R_{net}) at the hourly and half-hourly time scale at the majority of measurement sites (Baldocchi et al. 2001; Wilson et al. 2002; Foken et al. 2010). This imbalance is either due to errors in measurement or a result of invalid assumptions (Twine et al. 2000). The measurement errors stem from instrumental limitations and difference in footprint of the sensors. For instance, while the footprint of measurement of the energy fluxes is variable, that of the net radiometer is much smaller and remains constant throughout the observation period. Similarly, the ground heat flux has a small footprint and is affected by the local heterogeneity in soil conditions. However, these measurements errors are usually small and not enough to explain the residual of the surface energy budget (Foken 2008). Another reason for the imbalance is the lack of detection of energy storage by the eddy covariance method. The air and vegetation can store and release energy, which may account for part of the energy imbalance. Leuning et al. (2012) showed that the high imbalance in the daytime energy balance is due to a lack of consideration of the energy storage terms, and the closure fraction gets significantly reduced when daily averages are used instead of 30-min averages. During stable conditions or due to strong advection, the assumption of fully turbulent transport is not valid (Oncley et al. 2007), which could cause some of the energy imbalance. Lastly, mesoscale circulation caused by landscape heterogeneity can lead to the underestimation of the energy fluxes, which implies that a single eddy covariance tower and 30-min averaging periods are not enough to fully measure the fluxes (Stoy et al. 2013). Given the different possible reasons for this energy balance non-closure, the residual of the energy imbalance is attributed to either H, or LE, or both using different methods, commonly termed as post-closure methods (see Sect. 2.6) (Twine et al. 2000). This dual-uncertainty in measurements and model simulations further complicates the process of understanding land-atmosphere interactions.

Since the surface fluxes represent the lower boundary conditions in global-circulation as well as regional-weather models (Pitman 2003), better representation of surface energy flux partitioning is essential to improve numerical weather prediction (NWP) and understand the significance of land-atmosphere interactions on changes in weather and climate. It is also becoming evident that slight variations in land-atmosphere interactions at the local scale can have important regional effects (Pitman 2003). Thus, before relying on regional weather models as accurate prognostic tools, it is imperative that the uncertainty in partitioning the surface fluxes by LSMs be reduced, as also suggested by Davin et al. (2016). It is difficult to evaluate LSMs at larger scales due to the lack of accurate, large-scale spatial data; there are also disparities between grid-averaged model results and point-scale observations. However, testing one-dimensional (1D) or point models at the local scale using networks of observing stations can minimize this scale mismatch and allow us to test the accuracy of representing physical and biological processes in these models.

The Indo-Gangetic Basin, situated in the northern part of India, is one of the most populous river basins in the world (Sharma et al. 2010). A major portion of the economy of this region is driven by agriculture, which is particularly vulnerable to monsoonal rainfall variability (Siderius et al. 2014). The flux of sensible heat from the warm land surface during pre-monsoon period (March to June) creates a low pressure region over the Indo-Gangetic Basin, inducing the flow of moist air from the Indian Ocean (Yamashima et al. 2015). As such, land-atmosphere interactions have a significant impact on the strength and variability of the South-Asian monsoon. A modelling study found that there is a strong coupling between large-scale monsoonal rainfall with soil moisture through H (Unnikrishnan et al. 2017). Another study linked the post-1950s weakening in the South-Asian monsoon circulation to reduced evapotranspiration driven by large-scale deforestation in India (Paul et al. 2016). Both of these studies used the Weather Research and Forecasting (WRF) model, which has been shown to have a dry bias over the Indo-Gangetic Basin (Tang et al. 2016). Several studies related to the Global Land-Atmosphere Coupling Experiment (GLACE) using 12 general circulation models (GCMs) found that during the boreal summer, North India is one of the global hotspots for land-atmosphere coupling (Koster et al. 2004; 2006; Guo et al. 2006). The land-atmosphere coupling in this region also has local-scale implications. For instance, after the monsoon onset, the ratio of H to LE (the Bowen ratio, β) affects the variability in cloud formation (Chakraborty et al. 2015). Another study suggested that the difference in LE between urban and rural locations may strongly modulate the inter-seasonality of the surface urban heat island of cities in this region (Chakraborty et al. 2017). Knowing how these interactions affect the Indo-Gangetic Basin at different scales, as well as deciding on proper mitigation measures for possible future scenarios, require better predictive capacity of climate and weather models. Therefore, it is important to quantify how well LSMs can simulate the energy fluxes, since their accuracy will strongly influence the uncertainty in coupled model simulations over this region.

In the present study, eddy covariance measurements during the warmest part of the monsoon onset period of two consecutive years (2016 and 2017), spanning around 12 days (each), in central Indo-Gangetic Basin (see Fig. 1) are used to evaluate the Noah LSM (Mitchell 2005). Noah is used as the default land-surface module for a host of WRF model studies performed in India (Mohan and Bhati 2011; Panda and Sharan 2012; Samala et al. 2013; Vishnu and Francis 2014). However, there is a dearth of validation studies on Noah LSM for Indian conditions. Previous studies on evaluating Noah LSM in India have missed important variables that influence the surface energy balance, such as skin temperature and R_{net}, in their analysis (Bhattacharya and Mandal 2015) or have not evaluated the model using direct measurements of *LE* (Patil et al. 2014). Moreover, they have not investigated the influence of measurement uncertainties on such model evaluations.

The major research questions addressed by this study are:
1. What is the magnitude of the current biases in Noah simulations over the central Indo-Gangetic Basin?
2. How do site-specific parameters improve model simulations?
3. To what extent do post-closure methods alter model-data comparisons?

Significant biases are seen in the modelled partitioning of energy fluxes over this region during the study periods represented in the Global Land Data Assimilation System (GLDAS)/Noah dataset (Rodell et al. 2004) (Fig. S1). To investigate whether this is a problem of scale, simulations are performed for the site using a 1D version of the model. Better representation of vegetation and land surface properties were incorporated into Noah to quantify the effect of site-specific parameters on surface energy partitioning. Comparison of the observed partitioning with the results of a coupled run confirms that the biases in the Noah LSM, run with default parametrization, is actually magnified in coupled model runs over this region. Finally, the effect of three commonly used post-closure methods to partition the residual energy on model evaluation is investigated.

Site description and instrumentation, model run details, and data processing are described in Sect. 2, observations are shown in Sect. 3.1, the improvements in model simulations using site-specific land surface and vegetation parameters are discussed in Sect. 3.2.1, comparisons with coupled model results are presented in Sect. 3.2.2, and impact of post-closure methods are considered in detail in Sect. 3.2.3. Finally. the limitations and future scope of this study are discussed in Sects. 3.3 and 3.4, respectively.

2 Methodology

2.1 Site Description

All in-situ observations are made from a 10-m tall tower in the centre of a semi-natural grassland (refer to Fig. 1) located in the western portion of the Indian Institute of Technology, Kanpur (IITK) campus (26°30'32.72"N, 80°13'25.72"E). The grassland has an average altitude of 132 m above sea level and an area of roughly 500 m $\times$ 500 m (25 hectares). This measurement site is a part of the Indo-UK Interaction of Convective Organisation with Monsoon Precipitation, Atmosphere, Surface & Sea (INCOMPASS) project's flux tower network

(Turner et al. 2015). The fetch around the tower is representative of the non-agricultural grasslands in the Indo-Gangetic Basin and is dominated by wild elephant grasses (variants of *Pennisetum purpureum* and *Phragmites-Saccharum-Imperata*), plus other less common grasses and some shrubs, with canopy height varying from 0.2 m during the dry season to approximately 2.8 m during late monsoon. During the two study periods, the canopy height varied from 0.25 to 0.3 m. The soil texture in the field is silt loam with about 80% silt, 15% clay, and 5% fine sand (by weight). The soil type is Fluvisol (alluvium), with a pH of 8.3, and has very little organic content, with 0.82% Carbon and 0.29% Nitrogen by weight. The groundwater table in Kanpur varies between 10 and 20 m below ground level depending on season (Prasad et al. 2016), and there is surface water accumulation from irrigation overflow during December and July at the field site. Data collection is a challenge during pre-monsoon period, as intermittent wild fires disrupt continuous measurements (Sahu et al. 2015). For the present study, data are used from 1 – 12 May for 2016 and from 17 – 28 April for 2017. A large fire event occurred at the end of March in 2016 and removed the majority of the biomass from the field site, though it quickly recovered following the fire.

2.2 In-situ Measurements

All major components of the surface energy balance, which is given by

$$R_{\mathrm{net}} = H + LE + G_{\mathrm{s}}, \tag{1}$$

are measured at the study site.

As mentioned earlier, H is the sensible heat flux, LE is the latent heat flux, and G_{s} is the ground heat flux at the surface. R_{net} is the net radiation, which is given by

$$R_{\mathrm{net}} = L\downarrow + S\downarrow - L\uparrow - S\uparrow . \tag{2}$$

Here, $L\downarrow$ is the downwelling longwave radiation, $S\downarrow$ is the downwelling shortwave radiation, $L\uparrow$ is the upwelling longwave radiation and $S\uparrow$ is the upwelling shortwave radiation.

The eddy covariance tower has a Licor 7500 (LI7500) H_2O/CO_2 open-path gas analyser (LI-COR Biosciences, Logan Utah, USA) and a Gill Windmaster sonic anemometer-thermometer (Gill Instruments Ltd., Lymington, UK) to measure gas concentration and three-dimensional (3D) wind field at a frequency of 20 Hz. These sensors were mounted 5.28 m above the ground, and the LI7500 had a northward separation of 0.08 m, an eastward separation of 0.03 m, and a vertical separation of 0.27 m. Ambient temperature and relative humidity are measured using a HMP155 temp/RH probe (Vaisala, Vantaa, Finland) mounted at 4.5 m above the surface. In addition, two HFP01SC heat flux plates (Hukesflux, Delft, The Netherlands), kept 0.03 m below the surface, and a 4-component net radiometer (Hukesflux, Delft, The Netherlands), mounted 4.7 m above the surface, provide measurements of the available energy ($R_{\mathrm{net}} - G_{\mathrm{s}}$). Two sets of soil moisture/soil temperature measurements are made using digital time domain transmissometry (TDT) sensors (Acclima Inc., Meridian, Idaho, USA). The TDT sensors are at depths of 0.05 and 0.15 m below ground level and located underneath each heat flux plate. Wind speed and direction are measured at a height of 10 m above ground level using a Gill Windsonic two-dimensional (2D) anemometer (Gill Instruments Ltd., Lymington, UK). In addition, a Mobotix S15 camera (Mobotix, Winnweiler, Germany) is used to get photographs of the cloud cover and vegetation cover four times a day. A tipping bucket rain gauge (Environmental measurements Ltd., Newcastle, UK) is used to measure precipitation. All data are logged using a Campbell Scientific CR3000

Micrologger (Campbell Scientific, Logan, UT, USA). Other than the eddy covariance measurements, all variables are scanned at 0.1 Hz and logged as one-minute means (sums for rainfall). Note that there were a couple of rainy days during the study period of 2016 and no rain during that of 2017.

2.3 Data Processing

For 2016, *H* and *LE* were computed with a missing sample allowance of 10% using the EddyPRO software after removing spikes and implausible values from the raw time series (Vickers and Mahrt 1997; Mauder et al. 2013). The sonic anemometer data were corrected using 2D coordinate rotation (Wilczak et al. 2001) and angle of attack correction (Nakai and Shimoyama 2012). Block averaging was used to compute the fluxes, followed by high- (Moncrieff et al. 1997) and low-frequency spectral attenuation correction (Moncrieff et al. 2004). *H* was corrected for the influence of water vapour (Schotanus et al. 1983; Liu et al. 2001), while *LE* was corrected for air density variations (Webb et al. 1980). Statistical outliers were removed for both *H* and *LE* (Papale et al. 2006). In addition, absolute limits for all measured variables were defined to minimize instrumental errors and data were ignored when the signal strength of the LI7500 was below 80%. The CarboEurope flagging scheme described in Mauder and Foken (2011) was used to determine the best quality surface energy flux data. Finally, a fully-spatial analytical footprint analysis was performed at the thirty-minute time scale to assess the representativeness of the measured fluxes (Neftel et al. 2008).

Due to data logger errors, raw data were not available for 2017. So, gap-filled data were used for the analyses (Reichstein et al. 2005). Because of the lack of high-frequency data, a similar footprint analysis could not be performed for the second year.

Since ground heat flux is not measured at the surface, the heat stored above the heat flux plate was calculated using a numerical calorimetric approach (Liebethal et al. 2005). The soil heat storage, S_s, is given by

$$S_\mathrm{s} = \frac{\Delta T_\mathrm{s}}{\Delta t}(\rho_\mathrm{s} C_\mathrm{s} + q_\mathrm{v} \rho_\mathrm{w} C_\mathrm{w})\Delta z. \tag{3}$$

Here, ΔT_s is the change in soil temperature in K (at 0.05 m) over a time interval Δt (30 min in this case), ρ_s is the bulk density of the dry soil in kg m^{-3}, C_s is the specific heat capacity of the dry soil in J kg^{-1} K^{-1}, q_v is the measured volumetric moisture content at 0.05 m in m^3 m^{-3}, ρ_w is the density of water in kg m^{-3}, C_w is the specific heat capacity of water in J kg^{-1} K^{-1}, and Δz is the depth over which the heat storage is calculated (0.03 m in this case).

The bulk dry density of the soil is 1525 kg m^{-3} based on field measurements, specific heat capacity of dry soil is assumed to be 840 J kg^{-1} K^{-1} since it has very little organic content (Hanks and Ashcroft 1980), and that of water is 4184 J kg^{-1} K^{-1}.

G_s is given by

$$G_\mathrm{s} = G + S_\mathrm{s}, \tag{4}$$

where *G* is the measured ground heat flux.

2.4 Noah LSM Description

Originating from the Oregan State University (OSU) LSM, the Noah LSM has undergone a host of improvements and additions once it started being used by National Centers for Environmental Prediction (NCEP) in their general circulation model. The basic surface energy balance equation in the model is (1). The R_{net} values are calculated for each time step from the forcing values of $S\downarrow$ and $L\downarrow$, pre-defined albedo values, and $L\uparrow$ derived from skin temperature (T_{skin}). T_{skin} is calculated using a simple linearized formulation (Mahrt and Ek 1984). The available energy is then partitioned into H and LE. H is determined by the bulk heat transfer formulation (Garratt 1993), G_{s} is estimated using Fourier's law, and LE is obtained using Penman-derived potential evaporation formulation (Mahrt and Ek 1984). In the current version, the model has one canopy layer and four soil layers (Ek et al. 2003). More details about the model can be found in Chen et al. (2001).

For the 1D model evaluation, the latest version (3.4.1) of the uncoupled Noah LSM was run offline from 28 April to 12 May for 2016 and from 17 to 28 April for 2017. The model takes air temperature, humidity, wind speed, wind direction, surface pressure, precipitation, $S\downarrow$, and $L\downarrow$ as forcing variables. All the data were available every 30 min, and the model output was also in 30-min intervals. Four soil layers of 0.1 m, 0.1 m, 0.3 m, and 0.6 m were used for the simulations. Assuming that the 0.05 m TDT measurements are for the first 0.1 m layer and the 0.15 m TDT measurements are for the second 0.1 m layer, the model was initialized using soil temperature and soil moisture measurements for those layers (henceforth, T_{s1}, T_{s2}, q_{v1}, and q_{v2}), while linear extrapolation was used for the third and fourth layers. Though soil temperature and soil moisture may not linearly change with depth, since the extrapolated values are very close to the field values, the initial conditions have very little effect on the simulated T_{s1}, T_{s2}, q_{v1}, and q_{v2} after a couple of time steps. Since the LE data were missing for the first couple of days of the model run period in 2016, the data until 1 May 2016 were not used in the evaluation. T_{skin} used to initialize the model was derived from $L\uparrow$ following the Stefan-Boltzmann law, assuming a constant emissivity of 0.95 (Niemelä et al. 2001).

The first run (henceforth, NoahEX1) was made with the default parameters, with silt loam as the soil parameter and grassland as the vegetation parameter. Both of these choices were based on site conditions. Since NoahEX1 simulations showed large deviations from observations, to investigate the contributing factors, two more runs were performed (henceforth, NoahEX2 and NoahEX3).

For NoahEX2, the offline Noah model was constrained with observed values of radiative properties (albedo and emissivity) over the site. The default value of albedo was changed from 0.19 to 0.23 (lookup table: grassland) to the mean measured midday albedo value (0.165 for 2016 and 0.138 for 2017). Similarly, the surface emissivity was changed from 0.92 to 0.96 (lookup table: grassland) to 0.95 (value used to derive the skin-temperature from $L\uparrow$).

Since vegetation plays a major role in the moisture flux through transpiration, a third model run (NoahEX3) was performed after changing the vegetation properties. By default, the model has a very low vegetation cover for this period, with the fraction varying from 0.17 to 0.27 from April to May. Though only qualitative estimates were available for vegetation cover, the terrain photographs show that the vegetation covered more than half the field. So, the vegetation cover was changed from 0.5 to 0.6 for this run. The leaf area index (LAI) for grassland in the model is varies from 0.52 to 2.10 by default. Since the grassland site is primarily covered by grass of 0.25 to 0.30 m height during the study periods, the LAI for this site may be different. An LAI-2000 plant canopy analyzer (LI-COR Biosciences, Logan Utah, USA) was used to measure the *LAI* around the eddy covariance site during this period in 2017. The *LAI* was 3.91 for short grasses and 3.53 for very short grasses. Since the site was dominated by a combination of these during the study periods, for NoahEX3, the *LAI* parameter was constrained to 3.73-3.75 for 2016 and to 3.7 for 2017, which should be reasonably close to the field values.

2.5 Criteria for Model Evaluation

To evaluate the model, three statistical parameters were used: the coefficient of determination (r^2), the root-mean-square error (*RMSE*), and the mean bias deviation (*MBD*).

The *RMSE*, which is a measure of the difference between the observed and predicted values, is given by

$$RMSE = \sqrt{(\frac{\sum_{i=1}^{n}(P-O)^2}{n})}, \tag{5}$$

where O is the observed value, P is the predicted value, and n is the number of data points.

Since *RMSE* does not show whether the model over or underestimates the observed values, the *MBD* was also determined, given by

$$MBD = \frac{\sum_{i=1}^{n}(P-O)}{n}. \tag{6}$$

Thus, a positive bias represents an over-prediction by the model, while a negative bias represents an under-prediction. All the data points available were used to evaluate R_{net}, $S\uparrow$, $L\uparrow$, T_{s1}, T_{s2}, q_{v1}, q_{v2}, T_{skin}, and G_{s}. To quality-assure the energy fluxes, only the data when 70% contribution of energy fluxes are from within the field site were considered for model evaluation for 2016. By doing so, the assumptions of a 1D model are satisfied. Moreover, only the highest quality of energy flux data (quality flag 0) based on the CarboEurope flagging system (Mauder and Foken 2011) were used for the evaluation. Since the dataset for 2017 did not include the raw data, there were not as many high quality data points and no footprint coverage. Thus, for 2017, the energy flux data with quality flags of 0 and 1 were used for the evaluation. It should be noted that the 2017 data were mainly used to verify whether the results we obtained for 2016 were consistent across two consecutive monsoon onset periods.

2.6 Post-Closure Methods

Where to assign the measured residual energy due to the non-closure is an important open question in this field (Foken 2008). One approach, known as the β post-closure approach, is to force closure by using the measured β (Twine et al. 2000). This assumes that the ratio of H and *LE* is same for the missing flux as the ratio detected by the eddy covariance system (Ruppert et al. 2006). However, this assumption may not be true. The contribution of large eddies, that cannot be detected for shorter averaging periods, may be dominated by *LE* or H. Another approach, called the *LE* post-closure approach, is to attribute the missing energy to *LE* (Falge et al. 2005). A previous study showed that by increasing the averaging period from 30 min to 24 h to 5 days, the residual completely disappeared (Mauder and Foken 2006).

Moreover, the study found that the residual was primarily caused by H. This predominance of H in the energy balance residual has also been found in a recent study for 6 land use types (Charuchittipan et al. 2014). Based on this, a third approach, known as the H post-closure approach, assigns the missing energy to H (Ingwersen et al. 2011).

A part of the difference between model simulations and observations could be due to the degree of closure achieved at the study site and the post-closure method employed (Ingwersen et al. 2015). In this study, all three approaches were used to investigate the impact of the post-closure approach on the model evaluation.

3 Results and Discussion

3.1 Observed Surface Energy Budget

Figure 2 shows the time series of observed R_{net}, H, LE, and G during the study periods in 2016 (Fig. 2a) and 2017 (Fig. 2b). Here, upwelling H and LE, and downwelling R_{net} are considered positive, while downwelling H and LE, and upwelling R_{net} are considered negative. G is positive when directed away from the surface (into the soil). All the times mentioned in the figures or text are local. Both years show similar patterns, with LE higher than H for the entire period. In 2016, the turbulent energy fluxes show comparable values on the 3rd, 4th, and 5th of May. There has not been a lot of work on the partitioning of the energy fluxes over India during the monsoon onset period. A previous study over a suburban eddy covariance station in Lucknow, situated in the northern part of the Indo-Gangetic Basin, found that maximum daytime LE (142 ± 84 W m^{-2}) was slightly higher than H (130 ± 82 W m^{-2}) during pre-monsoon (Venkata Ramana et al. 2004). The study did not look at the energy balance closure (EBC) due to unavailability of R_{net} and G measurements. Another study used the β energy balance method over an irrigated ecosystem in Eastern India and found that the magnitude of LE was three to four times that of H during pre-monsoon (Kar and Kumar 2007).

For the next part of the study, G_{s} was calculated after accounting for the storage term, S_{s}. For 2016, during midday, mean S_{s} is -14.2 W m^{-2}, which is about 22% of the magnitude of the measured G (midday mean of 63.6 W m^{-2}). For midnight (2200 to 0200), mean S_{s} is 4.8 W m^{-2}, approximately 36% of the magnitude of the measured G for the same time period (-13.4 W m^{-2}). For 2017, the mean midday and midnight S_{s} are -7.8 W m^{-2} and 2.8 W m^{-2}, respectively. For this period, the storage accounts for 16% of the measured G during midday and and 43% of G during midnight. Figure 3a and 3b show the regressions between the available energy and the sum of the turbulent fluxes ($H + LE$) using 30-min averaged data for both years. The values during the day are in yellow, while those during the night are in violet. The slope of linear regression is 0.79 for 2016 and 0.77 for 2017, while the determination coefficient r^2 is 0.96 for 2016 and 0.97 for 2017. When the regressions are performed using daily averaged data instead (refer to Fig. 3c and 3d), the slope of the linear regression increases to 0.85 for 2016 and 0.92 for 2017. This is due to the impact of the storage terms on the surface EBC. During the day, there is a large energy imbalance since a part of the residual energy is stored in the vegetation, the soil (which is taken into account here), and the canopy air underneath the sensors. During the night, this energy is released, leading to a $H + LE$ greater than the available energy, as indicated by the violet points in Fig. 3a and 3b.

Figure 4a is the mean diurnal cycle plot of observed H and LE, G_{s}, R_{net}, the energy imbalance, and the footprint of measurements for 2016. The bounded lines represent the standard deviation from the measured mean, hourly values. The mean R_{net} reaches a maximum value of 586.1 ± 128.2 W m^{-2} around local noon (1200). *LE* dominates during this period, with a maximum value of 286.3 ± 72.2 W m^{-2} at 1300. At the same time, *H* has a value of 119.7 ± 37.7 W m^{-2}, making the β at this time approximately 0.42. The average G_S from the two soil flux plates at 1300 is 88.5 ± 24.4 W m^{-2}. The values for 2017 are very similar to 2016. The mean R_{net} peaks at noon, with a value of 637.7 ± 64.2 W m^{-2}. *LE* peaks at 1300 (322.7 ± 55.2 W m^{-2}), and β is 0.43. G_S at 1300 is 62.6 ± 3.8 W m^{-2}.

Figure 4a also shows the energy imbalance ($R_{\mathrm{net}} - G_{\mathrm{s}} - H - LE$) at the measurement site for 2016. As also indicated by Fig. 3a, the energy imbalance is maximum during the day, especially around noon, with a maximum value of 114.0 ± 121.9 W m^{-2} at noon. The energy imbalance is negative during night-time, i.e., the extra energy stored during the day is released, causing the turbulent fluxes ($H + LE$) to be higher than the available energy. Overall, the mean residual during the 2016 study period is 28.6 ± 60.5 W m^{-2}. For 2017, the residual flux is 135.6 ± 47.1 W m^{-2} at noon and has an overall mean of 19.0 W m^{-2}. It should be noted that the variability in the fluxes are much lower in 2017 compared to the previous year. This is because of the lack of cloudy and rainy days during this study period.

The diurnal variation of the footprint of energy flux measurements for 2016, as calculated using the fully-spatial footprint analysis is also shown in Fig. 4a. On average, over 90% of the turbulent fluxes originate from within the field during the day. At night, there is more contribution from outside the field. The minimum flux contribution from within the field site is seen at 0500 (65.5 ± 24.4%). Owing to a lack of raw data, a similar footprint could not be calculated for 2017.

3.2 Site-specific Parameters and Post-closure Approaches to Improve Simulated Energy Partitioning

The offline Noah LSM was run over the observation site for both years. To account for the energy imbalance in flux tower observations, the model was evaluated after correcting the observations using three commonly used post-closure approaches.

The mean value of β from 1000 to 1400 is determined for each day of the study period for the initial observation, the model runs, and after forcing closure of the surface energy balance using only quality-assured data. Figure 5 shows the box plot of the midday β for the study periods for each case (Fig. 5a for 2016 and Fig. 5b for 2017). The observations show a mean midday β of 0.41 in 2016 and 0.52 in 2017. NoahEX1 and NoahEX2 yield β values of over 3 for both years, while NoahEX3 simulations of β are closer to the observations. Finally, the post-closure approaches also result in high variability of energy flux partitioning (from 0.26 for the *LE* post-closure method to around 1 for the *H* post-closure method for 2016 and from 0.39 to 0.85 for 2017). This is partly because of the high residual energy during the midday. It should be noted that the *H* closure produces the closest value to the final model run (NoahEX3) for both years. The variability in β is much higher for 2016, especially with NoahEX1 and NoahEX2. This is because the model responds strongly to the forced precipitation, which is not a factor in 2017. The following subsections discuss the details of the evaluation results, the possible reasons for the improvements, and its implications for land-surface modelling in the Indo-Gangetic Basin.

3.2.1 *Offline Noah LSM Runs*

The diurnal variation of the modelled and observed components of the surface energy balance are shown in Fig. 6. For H and LE, each subsequent run reduces the discrepancies between the simulations and the observations, which is also seen in the time series of the quality-assured observed data and simulated values (refer to Fig. S1 and S2). For G_s, NoahEX1 and NoahEX2 show higher diurnal variability, which is fixed in NoahEX3. Not much difference is seen in R_{net} for the different Noah runs, and the values are close to observations in all cases. The simulations capture the time of the peak H quite well. For LE and G_s, the diurnal peak in the simulations is slightly before the peak in observations. NoahEX3 simulations underestimate the daytime G_s compared to NoahEX1 and NoahEX2, while improving the night-time simulations.

The scatter plots of the measured and simulated surface energy balance components are shown in Fig. 7. NoahEX3 simulations are closest to the observations, as also seen from the time series (refer to Fig. S1 and S2). For H, the slope of the regression improves from 2 in NoahEX1 to 1.6 in NoahEX3 for 2016 and from 1.7 to 1.2 for 2017. For LE, the slope is 0.36 in NoahEX1 and improves to 0.93 in NoahEX3 (improvement from 0.31 to 1 for 2017). For G_s, it changes from 1.1 to 0.65 in the final model run for 2016 and from 2 to 1.3 in 2017. For R_{net}, all the model runs perform quite well, though there is an improvement of the slope of the regression from 0.92 to 0.99 for 2016 and from 0.88 to 0.99 for 2017. It should be noted that Fig. 7c and 7d indicate that Noah LSM does not provide negative LE. However, our observations show cases of negative LE at our site, probably due to condensation during dew fall.

Table 1 shows the evaluation of R_{net}, $S\uparrow$,$L\uparrow$, T_{s1}, T_{s2}, q_{v1}, q_{v2}, T_{skin}, H, LE, and G_s for all the offline Noah model runs for 2016, while Table 1 shows the corresponding results for 2017. The mean of the simulated values for each model run is also shown. The quality assurance of the flux data based on footprint coverage, combined with the low canopy height, removes almost all of the night-time values for 2016. Using night-time data for validation of modelled energy fluxes can significantly reduce the *RMSE* and *MBD* (since H and LE are very small in magnitude during the night). This cannot provide a complete picture of the midday energy flux partitioning and the biases in the model. This issue is prevalent in many studies, with both daytime and night-time flux data being used for the error calculation (Patil et al. 2014). Employing this criterion in the 2016 dataset leads to the higher *RMSE* compared to previous studies. However, this approach provides better indication of the midday biases for Noah-simulated heat and moisture fluxes. Moreover, the use of simulated data corresponding to quality-assured measurements leads to higher mean values for H and LE due to the predominance of daytime values. In comparison to the 2016 case, the quality control of the flux data did not involve screening for footprint coverage of the measured fluxes in 2017. Thus, the *RMSE*, the *MBD*, as well as the mean of the modelled fluxes are lower in 2017, even though the peak daytime values are very similar for both the years (refer to Fig. 4).

For NoahEX1, the diurnal variation in R_{net} is well captured by the model (r^2=1) (refer to Fig. 6g and 6h). This is partly because the R_{net} is forced by the measured $S\downarrow$ and $L\downarrow$. However, the model underestimates the R_{net} (*MBD* = -20.8 W m^{-2} for 2016; -31.2 W m^{-2} for 2017), due to an overestimation of both $S\uparrow$ (*MBD* = 11.8 W m^{-2} for 2016; 19.7 W m^{-2} for 2017) and $L\uparrow$ (*MBD* = 7.6 W m^{-2} for 2016; 10.0 W m^{-2} for 2017). The model significantly over-predicts the soil temperature at both depths (*MBD*=4.0 K for T_{s1} and 3.0 K for T_{s2} in 2016; 6.3 K for T_{s1} and 4.6 K for T_{s2} in 2017; p-value for two-sample t-test between observed and modelled values$<$0.001). T_{skin} is also overestimated, though to a lesser extent

(*RMSE*=2.1 K for 2016; 2.8 K for 2017). The variation in T_{skin} is better captured by the model (r^2=0.98 and 0.96 for 2016 and 2017) compared to that of T_{s1} or T_{s2}. The average magnitude of the soil moisture is well-predicted by the model (*MBD*=4.0% for q_{v1} and 2.3% for q_{v2} in 2016; 0.3% for q_{v1} and 3.5% for q_{v2} in 2017). However, the model cannot capture the variation of soil moisture well in most cases (r^2=0.45 for q_{v1} and 0.41 for q_{v2} in 2016; 0.17 for q_{v1} and 0.95 for q_{v2} in 2017).

The simulated H is significantly higher than the measurements (*MBD*= 104.3 W m^{-2} for 2016; 52.9 W m^{-2} for 2017; p-value for two-sample t-test between observed and modelled values$<$0.001), while *LE* is significantly lower (*MBD*=-89.07 W m^{-2} for 2016; -61.57 W m^{-2} for 2017; p-value for two-sample t-test between observed and modelled values$<$0.001). G_{s} shows a very low *MBD* (-5.00 W m^{-2} for 2016; -0.5 W m^{-2} for 2017) with a much higher *RMSE* (19.0 W m^{-2} for 2016; 34.5 W m^{-2} for 2017). This suggests that the diurnal variation of G_{s} is much more pronounced in the model, with both positive and negative deviations from the observed values, as seen in Fig. 6e and 6f. Overall, the model overestimates H (by 279% in 2016 and by 108% in 2017) and underestimates *LE* (by 56% in 2016 and by 67% in 2017). For 2016, the midday β is 3.09; much higher than the observed midday β of 0.41. For 2017, the simulated midday β is 3.23 versus the lower observed β of 0.52.

The evaluation of the NoahEX1-simulated variables confirm that there are still a number of notable issues with the model. This is in agreement with previous work on offline Noah model evaluations (Velde et al. 2009; Ingwersen et al. 2011). A study in Nebraska found that the model performed poorly during wet periods, with an enhanced diurnal range in soil temperature, overestimation of peak H by 57% and underestimation of *LE* by 50% due to the effect of sub-surface water (Radell and Rowe 2008). A study in the Tibetan plateau compared three default parametrizations in Noah model during a dry week and found similar results to the results presented here, i.e. the surface partitioning was biased towards H (*MBD* =50 W m^{-2}) (Velde et al. 2009). In another study, simulations with constant minimum canopy resistance were compared to those with time varying minimum canopy resistance for a wheat field in Germany (Ingwersen et al. 2011). The study showed that the biases in the flux simulations depended on the stage of crop growth, with the model overestimating *LE* and underestimating H during the fruit-ripening stage and the opposite happening before the ripening period.

Very few studies have been performed on the evaluation of the offline Noah model in India. An evaluation study at a semi-arid site in India found an overestimation of soil temperature by Noah during the Indian monsoon, with an underestimation during the pre-monsoon period (Patil et al. 2011). Another study compared Noah model simulated soil temperature to observations for dry and wet periods for four semi-arid sites of the LASPEX experiment. They found a similar overestimation, with the *RMSE* for the temperature of the top soil layer ranging between 1.8 and 4.8 K (Waghmare et al. 2012), while the *RMSE* for R_{net} varied between 36.6 and 76.6 W m^{-2}. A recent study used 1 year of soil temperature data for two sub-tropical sites and also found that the soil temperature was consistently overestimated by the model for the first layer (*RMSE*=1.5 to 2 K)(Bhattacharya and Mandal 2015). All three studies found that the simulated soil temperature improve for the deeper layers, with *RMSE* reducing with depth, which is also seen in the present study. The energy fluxes have not been evaluated in depth for India. While two of the studies used measured H to evaluate Noah model, they did not have direct measurements of moisture flux. One study found a significant overestimation of H for a sub-tropical site, with *RMSE* greater than 100 for all periods (Patil et al. 2014). The other study, which was for the semi-arid site, found that Noah-simulated H was almost double the observed midday values for the wet period, with no observed data available for the dry period (Patil et al. 2011).

The bias in R_{net} for 2016 is reduced from -20.8 W m^{-2} in the NoahEX1 to -9.7 W m^{-2} in NoahEX2 (refer to Table 1). Moreover, the regression is closer to the 1:1 line (refer to Fig. 7g). This is primarily because the lower albedo increases the R_{net} (from an overall mean of 138.1 W m^{-2} to 149.2 W m^{-2}) by reducing $S\uparrow$ (from 55.5 W m^{-2} to 41.6 W m^{-2}). However, the increasing R_{net} also increases T_{skin} (from 306.9 K to 307.1 K), and thus $L\uparrow$ (from 498.0 W m^{-2} to 501.6 W m^{-2}), T_{s1} (from 306.1 K to 306.3 K), and T_{s2} (from 304.7 K to 304.9 K). It also slightly reduces q_{v1} (from 16.1% to 16.0%) and q_{v2} (from 17.5% to 17.4%). The increased surface emissivity would reduce the R_{net} and would have opposite effect on T_{skin}, T_{s1}, T_{s2}, q_{v1}, and q_{v2}. However, the effect of the change in albedo dominates in this case. With the increase in available energy, T_{skin}, T_{s1}, and T_{s2}, the difference between the forced air temperature and the modelled T_{skin} increases, thus increasing the overestimation of H. On the contrary, the bias in *LE* decreases due to the higher *LE* in this simulation. The patterns seen in the 2017 simulations are similar, albeit showing different magnitudes of change.

The use of site-specific vegetation parameters – in addition to realistic albedo and emissivity – in NoahEX3 significantly improves the results compared to NoahEX2. *LE* is predicted well by the model (*RMSE*=47.1 W m^{-2} and *MBD* =1.0 W m^{-2} in 2016; 33.3 W m^{-2} and 2.8 W m^{-2} in 2017). The overestimation of H is also reduced (*MBD*=62.1 W m^{-2} in 2016; 18.4 W m^{-2} in 2017), though the *RMSE* is still high. While R_{net} now has a positive bias (*MBD*=2.1 W m^{-2} in 2016; 0.8 W m^{-2} in 2017), the *RMSE* and *MBD* are smaller than that for NoahEX1 and NoahEX2. The temperature values are also improved, with lower bias for T_{s1} (*MBD*=4.2 K in NoahEX2 versus *MBD*=2.0 K for NoahEX3 in 2016; 6.7 K in NoahEX2 versus 4.2 K for NoahEX3 in 2017), T_{s2} (*MBD*=3.2 K in NoahEX2 versus *MBD*=0.7 K for NoahEX3; 4.9 K in NoahEX2 versus 2.3 K for NoahEX3 in 2017) and T_{skin} (*MBD*=2.0 K in NoahEX2 versus *MBD*=0.1 K for NoahEX3; 2.6 K in NoahEX2 versus 0.3 K for NoahEX3 in 2017), possibly due to higher rates of evaporative cooling. The small overestimation of R_{net} in this run is because of the lower $S\uparrow$ (*MBD* = -2.1 W m^{-2} in 2016; -2.3 W m^{-2} in 2017) and $L\uparrow$ (*MBD* = -0.8 W m^{-2} in 2016; 1.0 W m^{-2} in 2017).

3.2.2 Propagation of LSM Biases into Coupled Simulations

In addition to the issues with the 1D version of the Noah model run with default configuration for this study (NoahEX1), we also find that the GLDAS dataset, in which the Noah model is forced at a global scale, shows similar severe underestimation of *LE* and overestimation of H during this period (refer to Fig. S1). Running Noah model in an uncoupled mode cannot accurately predict how these biases will translate to errors in coupled modes. We expect that while coupled simulations will show the same patterns (overestimation of H and underestimation of *LE* when not using site-specific vegetation parameters), running LSMs in coupled versus uncoupled modes would have an impact on the magnitude of the simulated fluxes (and thus, the β), as also seen by Nemunaitis-Berry et al. (2017) for Oklahoma city. To confirm this hypothesis, we compare our results with the High Asia Reanalysis (HAR) dataset (Maussion et al. 2014).

The HAR dataset is based on WRF model runs over Asia at 30 km x 30 km resolution and uses Noah LSM as its land component. We use the data at the daily scale from 2010 to 2014 for the grid encompassing our study area. Figure 8 shows the daily mean β from the HAR data, the observed data for the two study periods, and the corresponding NoahEX1 runs for those periods. The NoahEX1 results for only those points that are also present in the observed dataset after quality control are used to calculate the daily means. As seen earlier in Fig. 5 for midday, the default uncoupled Noah model version significantly overestimates the daily mean β, with values ranging from 2 to 4 compared to observed values of less than 0.5. The first study period shows more variability in β due to the model's high sensitivity to rain events. The HAR dataset shows even higher values than the uncoupled model output, with β ranging from 3 to 6. The HAR reanalysis is constrained using the Operational Model Global Tropospheric Analyses and is not a true regional-scale reanalysis. Thus, forcing the Noah model using 30-min observed data at the field-scale expectedly shows improvement in the simulation of the energy flux partitioning compared to the WRF-Noah modelled data in the HAR database. The combined analyses show that the biases in the Noah model extend far beyond uncoupled simulations and will impact the variables that are derived from the lower boundary conditions in coupled models.

3.2.3 Impact of Post-closure Approaches

In the first case, we force EBC based on the observed β for every 30-min interval. Since the 2017 data have a lot of night-time values, which lead to negative β, and absurd H and LE after forced closure, all the data points with $\beta < 0.8$ were removed for this period. On average, the β closure leads to the increase of the measured H (by 86.1% in 2016 and 76.0% in 2017) and measured LE (by 25.3% in 2016 and 55.5% in 2017). For the second case, the residual is assigned to LE, which increases the mean LE by 48.5% (in 2016) and 15.4% (in 2017) while H obviously remains unchanged. For the third case, the residual is assigned to H. This increases the mean H by 197.7% (in 2016) and 64.9% (in 2017), while LE obviously remains unchanged. It should be noted that the final mean percentage increases were calculated using only those times when data were available for both the measured fluxes and the corrected fluxes after forcing closure.

Figure 9 shows the effect of the post-closure methods applied in the model evaluation. Decimal points are not shown for *RMSE* and *MBD* in the figure to conserve space. For H, both the *RMSE* and *MBD* decrease irrespective of the approach used. The improvement is most significant for the H post-closure approach. Since the discrepancy between the observed and NoahEX3-simulated variables is partly due to overestimation of H, assigning the entire energy balance residual to H has the greatest impact on model evaluation (*RMSE*=71.7 W m^{-2} and *MBD*=5.2 W m^{-2} for 2016; 39.1 W m^{-2} and -0.1 W m^{-2} for 2017). For the LE post-closure method, there should be no improvement for H, since the H values do not change. However, since the dataset is modified to remove the unrealistic values, the *RMSE* and *MBD* are slightly different. For the β approach, the improvement in *MBD* is minimal for 2016, but more significant for 2017. The highest r^2 is also found for the H closure (r^2=0.69 for 2016; 0.91 for 2017). For LE, the H post-closure method performs the best since the LE is not changed and Noah captures the magnitude and variation in LE after using site-specific vegetation parameters (*RMSE*=72.6 W m^{-2} and *MBD*=16.4 W m^{-2}; 33.3 W m^{-2} and 2.8 W m^{-2} for 2017).

3.3 Limitations of the Study

The NoahEX3 simulations may still lead to significant uncertainties. It is evident that the vegetation parameters have a major impact on the simulated LE. There was no site-specific measurements of stomatal resistance. Instead, the default values were used. Similarly, the vegetation cover derived from the MOBOTIX camera are only based on visual inspection. Higher stomatal resistance and lower vegetation cover would reduce the simulated LE and improve the correlation between simulated and observed values after post-closure. Since the *LAI* variation was constrained in the model runs (being set to 3.73) compared to the measured range (3.53 to 3.91), a sensitivity study was performed for both years to quantify *LAI* effect on the energy flux simulations (refer to Table T1). *LE* increases and *H* decreases due to higher *LAI*, which is expected. Increasing or decreasing *LAI* by 0.2 changes the mean *H* by less than 1%. The highest change is seen for *LE* in 2017, with an increase of around 3% due to an increase in *LAI* of 0.2. Thus, the uncertainty in specified *LAI* in the model runs has minimal impact on the simulated fluxes in this study.

The re-evaluation of the NoahEX3 simulations using three different post-closure approaches suggests that the approach can have a strong influence on the results of a model evaluation. While the *H* method provides the best match with the NoahEX3 simulations, it is important to note that it is unlikely that the residual energy only consists of sensible heat. There could be some contribution, though small, from *LE* (Mauder and Foken 2006). Thus, the diurnal variation of the heat flux is distorted by the artificial attribution of the residual energy to *H*. In summary, there are possibilities of misinterpretation in model evaluation studies when only one post-closure method is used, as also suggested by Ingwersen et al. 2015.

Though extending the averaging time for the EddyPRO processing can indicate how the missing energy is partitioned and improve the EBC, in this study, corrections are already made for the low-frequency co-spectral losses (Moncrieff et al. 2004). Moreover, a previous modified ogive analysis showed that 30 min is still the optimum averaging time for measurements over low vegetation (Charuchittipan et al. 2014).

Finally, forcing EBC at the 30-min time scale is not appropriate, since a complete EBC ignores heat storage (Leuning et al. 2012). While G_s is corrected for soil heat storage, heat storage in the biomass is ignored in the present study. Biomass storage depends strongly on the biomass content of the terrain, and has been shown to range from -50 to 50 W m^{-2} for temperate deciduous forests (Gu et al. 2007) and from -5 to 25 W m^{-2} for maize crop (Meyers and Hollinger 2004). By forcing the EBC, some bias is introduced into the model evaluation.

In the present study, we selected two short periods (12 days each) with continuous meteorological measurements during two consecutive years. The conditions prevalent during our study period and the site's surface properties are representative of the monsoon onset conditions in the Indo-Gangetic Basin. Nonetheless, these results do not necessarily imply that the Noah model has similar high biases in other period of the year. It is also possible that the change in phenology affects these biases during the other periods of the year.

3.4 Future Scope

Given the dearth of studies on evaluating LSMs in India, especially those using a complete suite of observations, it is imperative that large scale experiments be performed using multiple eddy covariance sites to investigate biases in the land-surface modules of global climate and regional weather models. These studies will improve understanding of land-atmosphere interactions in this region and lead to more accurate prediction of local weather and climate.

We show preliminary evidence that coupled simulations using default Noah model is heavily biased in this study region. The discrepancy in β simulation can affect both short- and medium-range weather forecasting. Moreover, it is important to examine whether these biases in modelled β may be contributing to the well-known problems that climate and numerical weather prediction models face when dealing with the South Asian summer monsoon (Turner and Annamalai 2012; Saha et al. 2014; Roxy et al. 2015).

Our findings are applicable to all places where seasonality or absolute vegetation properties are not accurately represented in the model's default parameterizations. Given the impact of site-specific parameters on LSM performance, widespread in-situ measurements are necessary in this region. Many of these parameters, like albedo, vegetation fraction, *LAI*, emissivity, etc. can be derived from satellite measurements, though evaluation is necessary for different scales (Glenn et al. 2008; Li et al. 2015). Other parameters, like surface roughness and stomatal resistance, are more site-specific. The data gathered from these studies can be used to update the existing lookup tables in Noah model (and other LSMs) and lead to future model development more suited to the ambient conditions of the Indo-Gangetic Basin.

4 Conclusions

The present study shows that the Noah LSM performs poorly over a grassland site in central Indo-Gangetic Basin during the monsoon onset period. Significant differences are found between observed (midday β of 0.41 for 2016 and 0.52 for 2017) and modelled (midday β of 3.09 for 2016 and 3.23 for 2017) energy fluxes, with H being significantly overestimated and LE being underestimated. Moreover, T_{skin}, T_{s1} and T_{s2} are all overestimated, while R_{net} is underestimated. These biases are amplified in coupled model runs that use Noah LSM as a land-surface module.

Running the model with modified land surface radiative properties slightly improves the R_{net} and LE estimates, but worsens the simulated T_{s1}, T_{s2}, and T_{skin}. The improvement in the prediction of almost all the variables when using site-specific vegetation parameters implies that these parameters, as defined in the model's lookup table, are not representative of the Indo-Gangetic Basin.

Forcing closure of the measured energy fluxes using three approaches, after accounting for heat storage in the soil, shows that part of the difference in model simulations and observations can be explained by the difference in EBC between the model and observations. Overall, attributing all the residual energy to H shows the greatest improvement.

In summary, significant biases are seen in Noah's simulated turbulent fluxes at multiple scales in this region during the monsoon onset period. Since Noah model is a default land-surface module in many numerical weather prediction models, these biases can cause uncertainty in coupled model simulations. Further work is needed to better parameterize vegetation properties in land-surface models in this region.

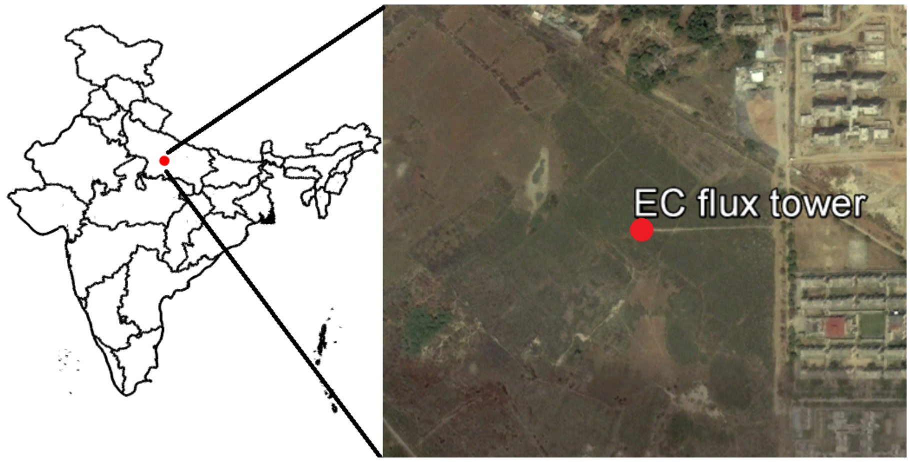

Fig. 1
Map of study area with position of the eddy covariance flux tower, with relative position of the study area within India in the inset. Image Courtesy: Google

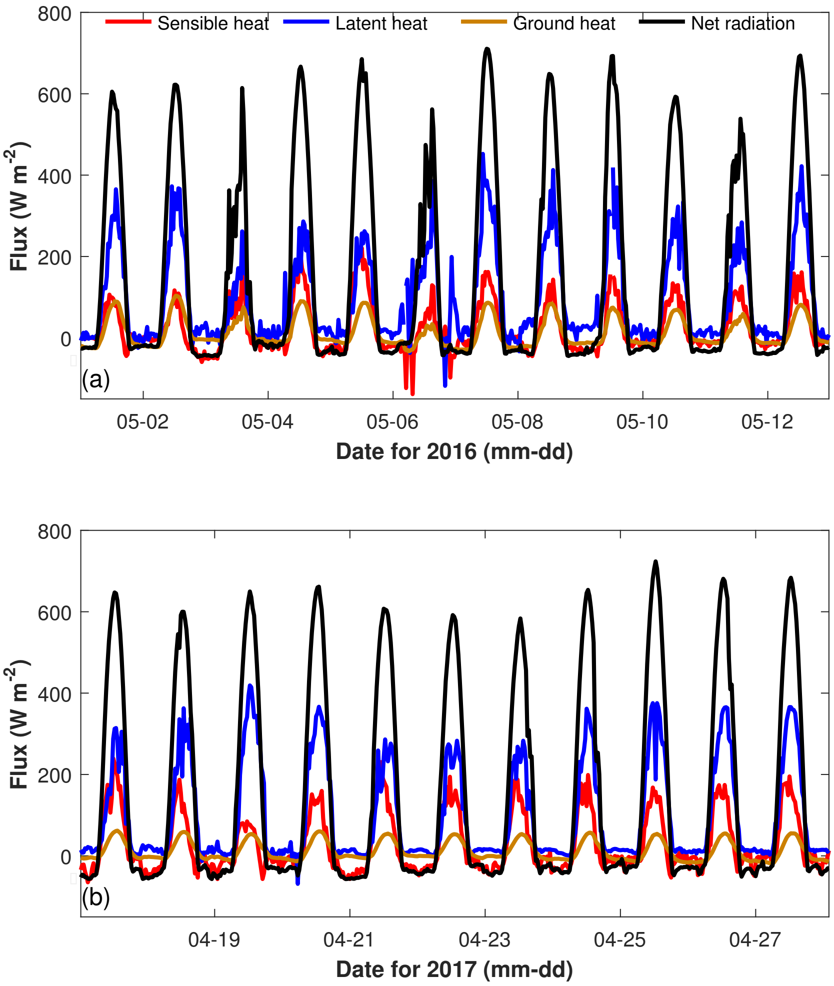

Fig. 2
Time series of observed surface energy budget terms during the **a** 2016 and **b** 2017 study periods. The dates are in the format, mm-dd

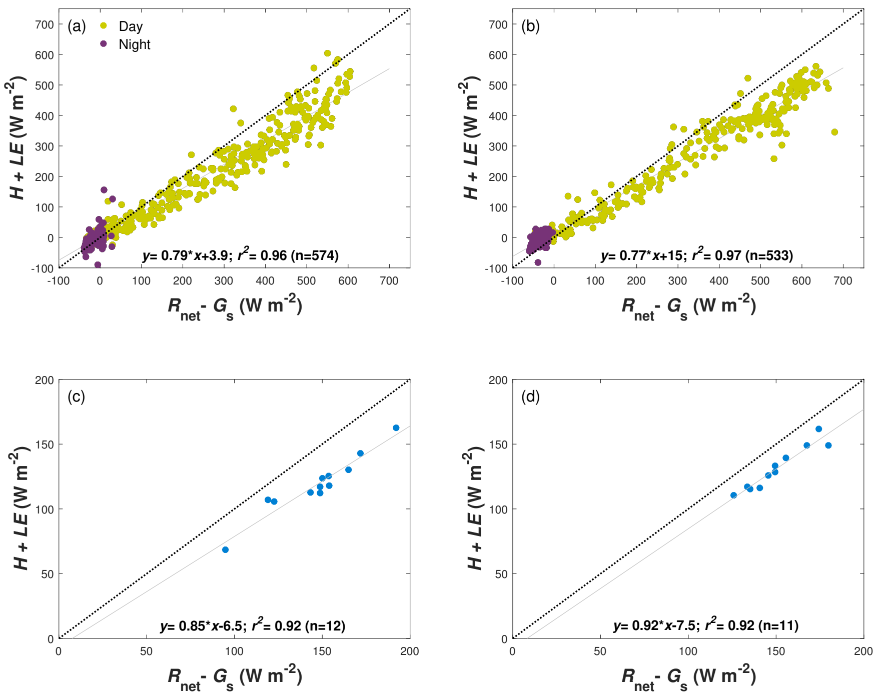

Fig. 3
Available energy ($R_{\mathrm{net}} - G_{\mathrm{s}}$) versus sum of energy fluxes ($H + LE$) using 30-min averages for **a** 2016 and **b** 2017 and daily averages for **c** 2016 and **d** 2017. The black dotted lines represent the reference lines with slopes of unity and n is the sample size

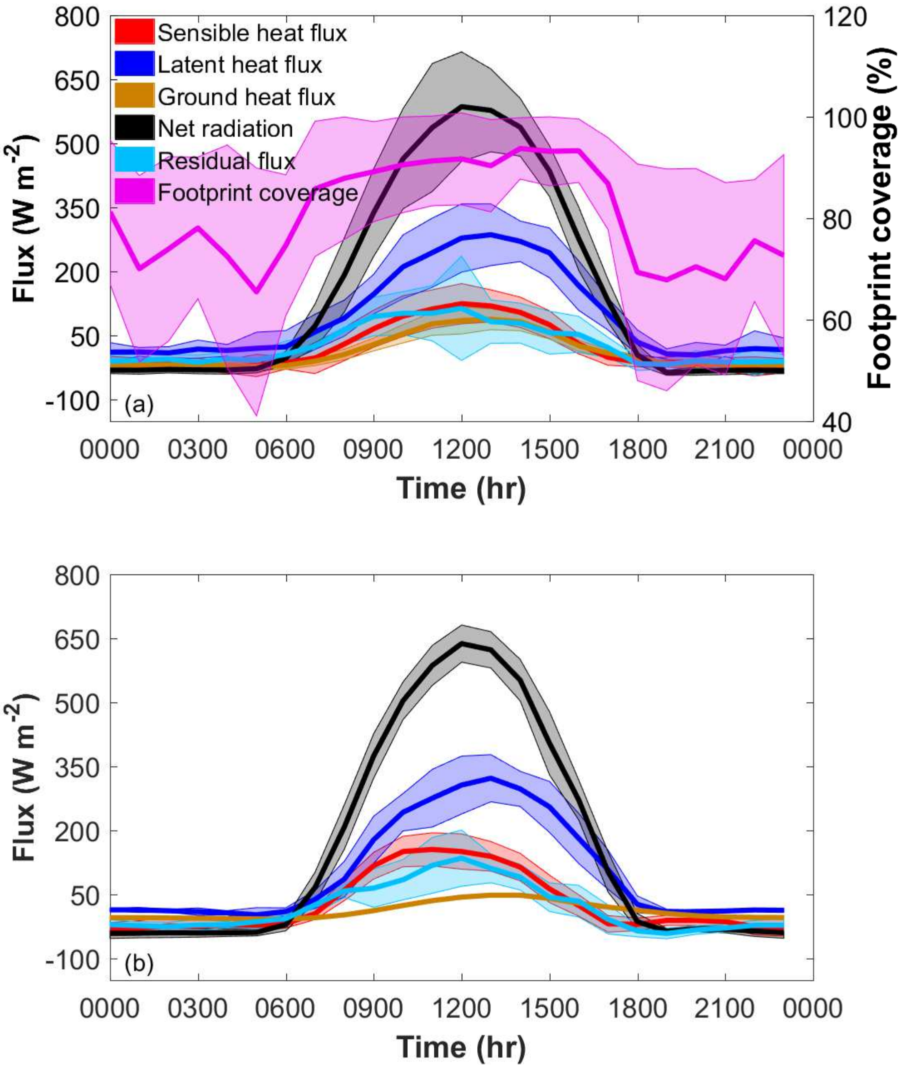

Fig. 4
Diurnal variation of measured H, LE, R_{net}, G_{s}, and residual energy flux for **a** 2016 and **b** 2017. The fraction of measured fluxes from field site is also shown for 2016. The solid lines represent the mean values, while the shaded areas represent the standard deviations

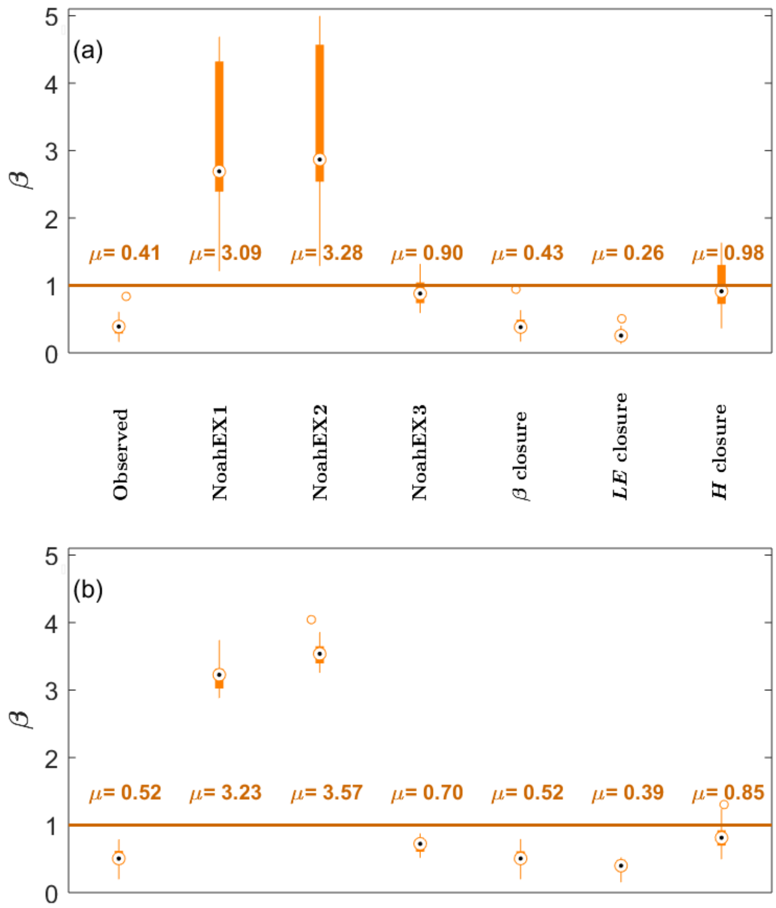

Fig. 5
Box and whisker plots of midday (1000 to 1400) β from initial observations, uncoupled Noah runs, and observations after forcing EBC for the study periods in **a** 2016 and **b** 2017. The horizontal line indicates a β of 1 and μ represents the mean β for each category. The vertical boxes span the interquartile range (25th to 75th percentile) with the dot showing the median value, and the whiskers extending to the maximum and minimum observations. The sample size is 94 for 2016 and 93 for 2017

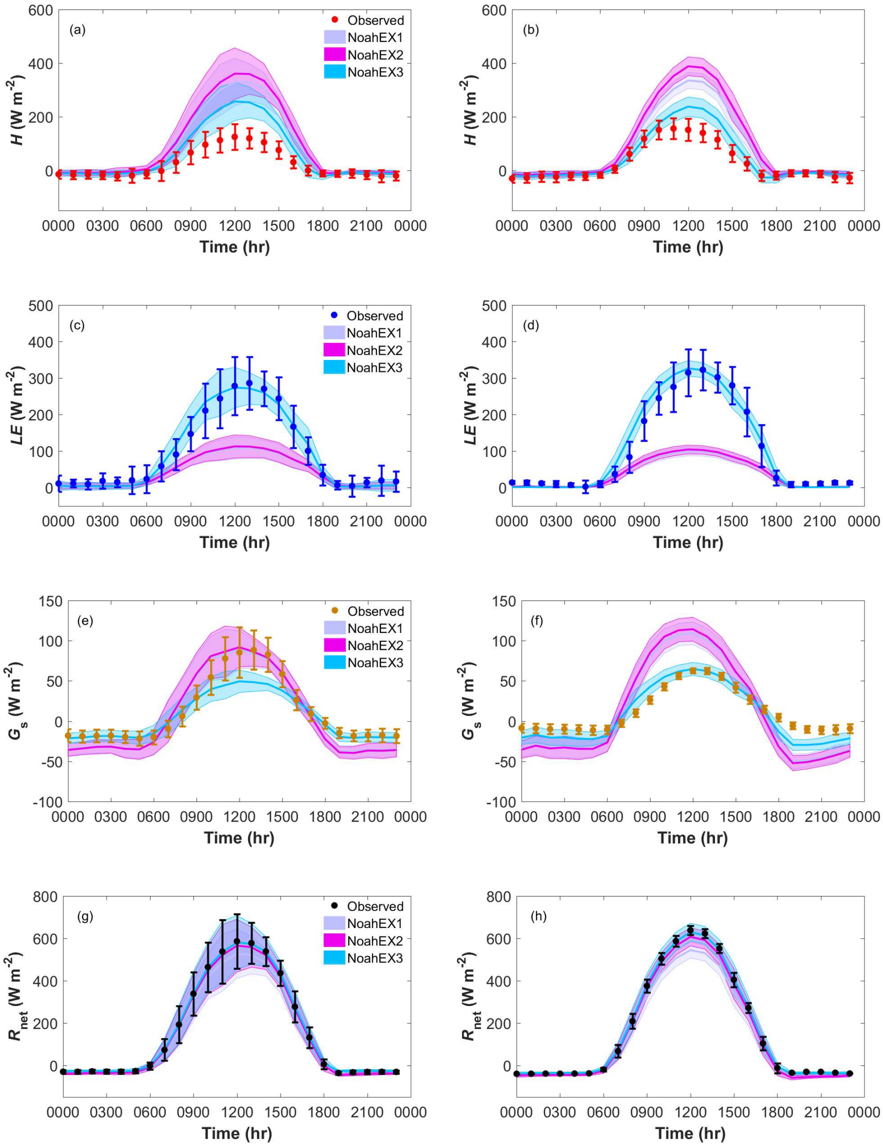

Fig. 6
Diurnal variation in offline Noah-simulated **a** H, **c** LE, **e** G_{s}, and **g** R_{net} for 2016 and **b** H, **d** LE, **f** G_{s}, and **h** R_{net} for 2017 against site observations. The dots and error bars are for the mean and standard deviation of observations, while the solid lines and shaded areas for the mean and standard deviation of the simulated data

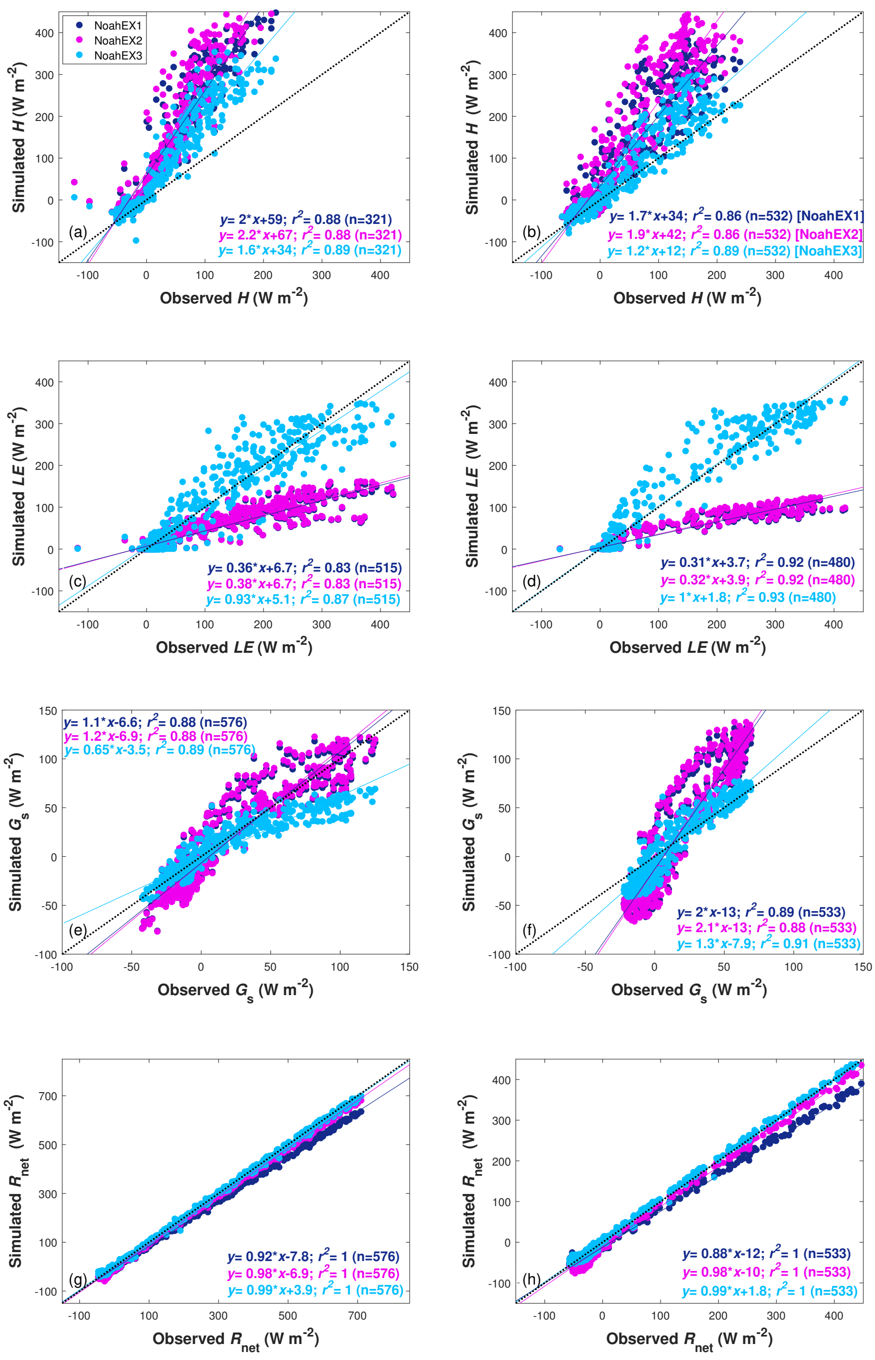

Fig. 7
Regressions of offline Noah-simulated **a** H, **c** LE, **e** G_{s}, and **g** R_{net} for 2016 and **b** H, **d** LE, **f** G_{s}, and **h** R_{net} for 2017 against site observations. The black dotted lines are the reference line with slopes of unity and n is the sample size

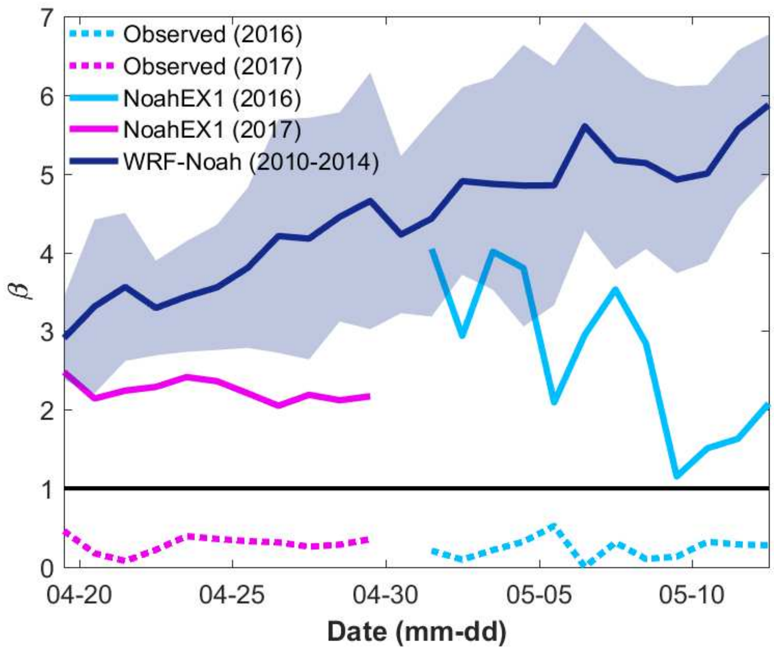

Fig. 8
Time series of daily mean β from observations, uncoupled Noah simulations, and coupled WRF-Noah model simulations from HAR. For HAR, the solid lines represent the mean values of 2010 to 2014, while the shaded areas represent the standard deviations. The horizontal line indicates a β of 1

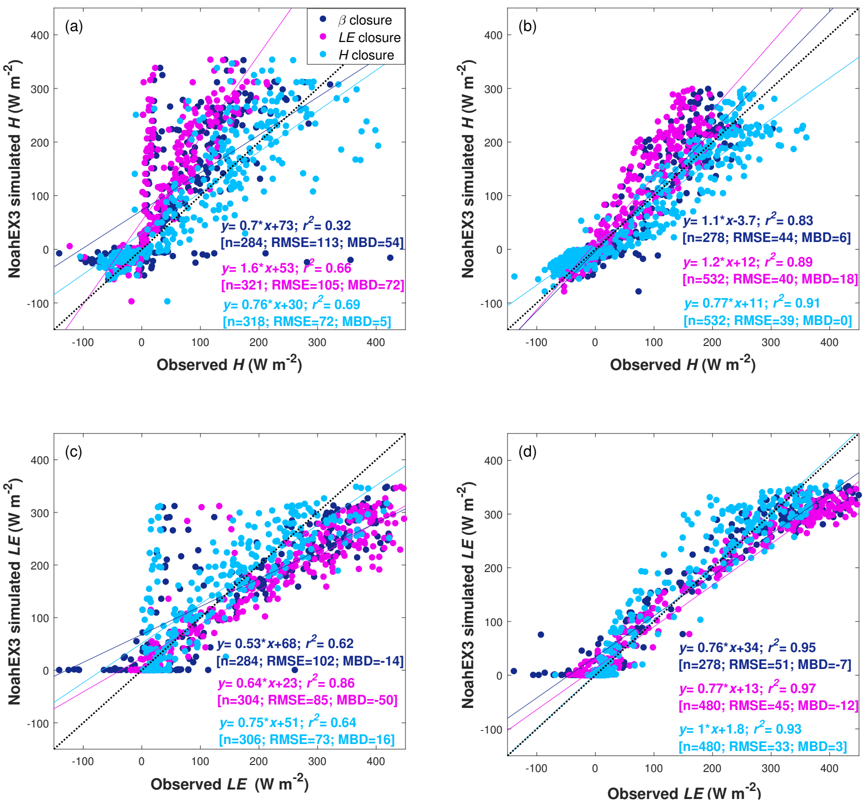

Fig. 9
Impact of three post-closure approaches on the evaluation of the Noah-simulated **a** *H* and **c** *LE* for 2016, and **b** *H* and **d** *LE* for 2017. The black dotted lines are the reference lines with slopes of unity and n is the sample size

Table 1: Evaluation of offline Noah simulations for 2016

	NoahEX1				NoahEX2				NoahEX3			
	Statistics											
Variable	Mean	r^2	*RMSE*	*MBD*	Mean	r^2	*RMSE*	*MBD*	Mean	r^2	*RMSE*	*MBD*
R_{net} (W m^{-2})	138.1	1.00	29.5	-20.8	149.2	1.00	12.7	-9.7	160.9	1.00	8.3	2.1
$S\uparrow$ (W m^{-2})	55.5	0.99	21.8	11.8	41.6	0.99	4.6	-2.14	41.6	0.99	4.6	-2.14
$L\uparrow$ (W m^{-2})	498.0	0.98	10.2	7.6	501.6	0.98	13.9	11.1	489.6	0.97	7.7	-0.8
T_{s1} (K)	306.1	0.86	4.4	4.0	306.3	0.86	4.6	4.2	304.2	0.87	2.3	2.0
T_{s2} (K)	304.7	0.79	3.0	3.0	304.9	0.79	3.2	3.2	302.4	0.67	0.9	0.7
q_{v1} (%)	16.1	0.45	4.8	4.0	16.0	0.44	4.7	3.9	14.3	0.12	3.2	2.2
q_{v2} (%)	17.5	0.41	2.6	2.3	17.4	0.40	2.6	2.3	14.0	0.03	1.4	-1.1
T_{skin} (K)	306.9	0.98	2.1	1.8	307.1	0.98	2.4	2.0	305.2	0.97	1.2	0.1
H (W m^{-2})	148.4	0.88	134.4	104.3	163.8	0.88	154.4	119.7	106.2	0.89	85.3	62.1
LE (W m^{-2})	65.2	0.83	117.0	-89.1	67.2	0.83	114.9	-87.1	155.3	0.87	47.1	0.98
G_s (W m^{-2})	-6.9	0.88	19.0	-5.0	-7.1	0.88	20.2	-4.8	-4.3	0.89	19.0	-7.6

Table 2: Evaluation of offline Noah simulations for 2017

	NoahEX1				NoahEX2				NoahEX3			
	Statistics											
Variable	Mean	r^2	*RMSE*	*MBD*	Mean	r^2	*RMSE*	*MBD*	Mean	r^2	*RMSE*	*MBD*
R_{net} (W m^{-2})	129.1	1.00	44.4	-31.2	146.8	1.00	18.2	-13.6	161.2	1.00	7.8	0.8
$S\uparrow$ (W m^{-2})	58.1	0.99	34.1	19.7	36.0	0.99	4.8	-2.3	36.0	0.99	4.8	-2.3
$L\uparrow$ (W m^{-2})	498.2	0.96	13.8	1.0	504.0	0.96	19.5	15.7	489.3	0.98	7.0	1.0
T_{s1} (K)	306.0	0.81	7.0	6.3	306.4	0.81	7.4	6.7	303.9	0.87	4.6	4.2
T_{s2} (K)	304.0	0.71	4.8	4.61	304.3	0.71	5.0	4.9	301.7	0.59	2.4	2.3
q_{v1} (%)	15.5	0.17	0.4	0.3	15.4	0.58	0.3	0.1	14.8	0.97	0.65	-0.48
q_{v2} (%)	21.5	0.95	4.0	3.5	21.5	0.95	4.0	3.5	17.4	0.91	1.0	-0.5
T_{skin} (K)	307.1	0.96	2.8	2.2	307.5	0.96	3.2	2.6	305.2	0.98	1.2	0.3
H (W m^{-2})	81.4	0.86	86.4	52.9	98.0	0.86	111.1	68.4	47.0	0.89	40.3	18.4
LE (W m^{-2})	32.6	0.92	105.8	-61.6	34.0	0.92	103.6	-60.1	97.0	0.93	33.3	2.8
G_s (W m^{-2})	-11.2	0.89	34.5	-0.5	-11.7	0.88	37.2	0.0	-6.9	0.91	13.5	-4.9

Acknowledgements We gratefully acknowledge the financial support given by the Earth System Science Organization, Ministry of Earth Sciences, Government of India (grant MM/NERC-MoES-03/2014/002) and Newton Fund to conduct this research under INCOMPASS campaign and Monsoon Mission. The INCOMPASS field campaign and A. G. Turner are supported in the UK by the NERC project NE/L01386X/1. Jonathan G. Evan's and Ross Morrison's work on this project was supported by the Centre for Ecology & Hydrology (CEH) and the National Environmental Research Council (NERC), UK. PNNL is operated for DOE by Battelle Memorial Institute under contract.

References

Abramowitz G, Pitman A, Gupta H, Kowalczyk E, Wang Y (2007) Systematic bias in land surface models. J Hydrometeorol 8(5):989–1001

Baldocchi D, Falge E, Gu L, Olson R, Hollinger D, Running S, Anthoni P, Bernhofer C, Davis K, Evans R, Fuentes J (2001) Fluxnet: A new tool to study the temporal and spatial variability of ecosystem-scale carbon dioxide, water vapor, and energy flux densities. Bull Am Meteorol Soc 82(11):2415

Bhattacharya A, Mandal M (2015) Evaluation of noah land-surface models in predicting soil temperature and moisture at two tropical sites in india. Meteorol Appl 22(3):505–512

Chakraborty S, Saha U, Maitra A (2015) Relationship of convective precipitation with atmospheric heat flux—a regression approach over an indian tropical location. Atmos Res 161:116–124

Chakraborty T, Sarangi C, Tripathi SN (2017) Understanding diurnality and inter-seasonality of a sub-tropical urban heat island. Boundary-Layer Meteorol 163(2):287–309

Charuchittipan D, Babel W, Mauder M, Leps JP, Foken T (2014) Extension of the averaging time in eddy-covariance measurements and its effect on the energy balance closure. Boundary-Layer Meteorol 152(3):303–327

Chen F, Dudhia J (2001) Coupling an advanced land surface-hydrology model with the Penn State-NCAR MM5 modeling system. part I: Model implementation and sensitivity. Mon Weather Rev 129(4):569–585

Davin EL, Maisonnave E, Seneviratne SI (2016) Is land surface processes representation a possible weak link in current regional climate models? Environ Res Lett 11(7):074,027

Ek M, Mitchell K, Lin Y, Rogers E, Grunmann P, Koren V, Gayno G, Tarpley J (2003) Implementation of noah land surface model advances in the national centers for environmental prediction operational mesoscale eta model. J Geophys Res Atmos 108(D22)

Entekhabi D, Asrar GR, Betts AK, Beven KJ, Bras RL, Duffy CJ, Dunne T, Koster RD, Lettenmaier DP, McLaughlin DB, Shuttleworth WJ (1999) An agenda for land surface hydrology research and a call for the second international hydrological decade. Bull Am Meteorol Soc 80(10):2043–2058

Falge E, Reth S, Brüggemann N, Butterbach-Bahl K, Goldberg V, Oltchev A, Schaaf S, Spindler G, Stiller B, Queck R, Köstner B (2005) Comparison of surface energy exchange models with eddy flux data in forest and grassland ecosystems of germany. Ecol Modell 188(2):174–216

Foken T (2008) The energy balance closure problem: an overview. Ecol Appl 18(6):1351–1367

Foken T, Mauder M, Liebethal C, Wimmer F, Beyrich F, Leps JP, Raasch S, DeBruin HA, Meijninger WM, Bange J (2010) Energy balance closure for the litfass-2003 experiment. Theor Appl Climatol 101(1-2):149–160

Garratt JR (1993) Sensitivity of climate simulations to land-surface and atmospheric boundary-layer treatments-a review. J Clim 6(3):419–448

Giorgi F, Avissar R (1997) Representation of heterogeneity effects in earth system modeling: Experience from land surface modeling. Rev Geophys 35(4):413–437

Glenn EP, Huete AR, Nagler PL, Nelson SG (2008) Relationship between remotely-sensed vegetation indices, canopy attributes and plant physiological processes: what vegetation indices can and cannot tell us about the landscape. Sensors 8(4):2136–2160

Gu L, Meyers T, Pallardy SG, Hanson PJ, Yang B, Heuer M, Hosman KP, Liu Q, Riggs JS, Sluss D, Wullschleger S (2007) Influences of biomass heat and biochemical energy storages on the land surface fluxes and radiative temperature. J Geophys Res Atmos 112(D2)

Guo Z, Dirmeyer PA, Koster RD, Sud Y, Bonan G, Oleson KW, Chan E, Verseghy D, Cox P, Gordon C, McGregor J (2006) GLACE: the global land-atmosphere coupling experiment. Part II: analysis. J Hydrometeorol 7(4):611–625

Hanks RJ, Ashcroft G (1980) Applied Soil Physics: Soil Water and Temperature Application. Springer Verlag, New York

Haughton N, Abramowitz G, Pitman AJ, Or D, Best MJ, Johnson HR, Balsamo G, Boone A, Cuntz M, Decharme B, Dirmeyer P (2016) The plumbing of land surface models: Is poor performance a result of methodology or data quality? J Hydrometeorol 17(6):1705–1723

Ingwersen J, Steffens K, Högy P, Warrach-Sagi K, Zhunusbayeva D, Poltoradnev M, Gäbler R, Wizemann HD, Fangmeier A, Wulfmeyer V, Streck T (2011) Comparison of noah simulations with eddy covariance and soil water measurements at a winter wheat stand. Agric For Meteorol 151(3):345–355

Ingwersen J, Imukova K, Högy P, Streck T (2015) On the use of the post-closure methods uncertainty band to evaluate the performance of land surface models against eddy covariance flux data. Biogeosciences 12(8):2311–2326

Jiménez C, Prigent C, Mueller B, Seneviratne S, McCabe M, Wood E, Rossow W, Balsamo G, Betts A, Dirmeyer P, Fisher J (2011) Global intercomparison of 12 land surface heat flux estimates. J Geophys Res Atmos 116(D2)

Kar G, Kumar A (2007) Surface energy fluxes and crop water stress index in groundnut under irrigated ecosystem. Agric For Meteorol 146(1):94–106

Koster RD, Dirmeyer PA, Guo Z, Bonan G, Chan E, Cox P, Gordon C, Kanae S, Kowalczyk E, Lawrence D, Liu P (2004) Regions of strong coupling between soil moisture and precipitation. Science 305(5687):1138–1140

Koster RD, Sud Y, Guo Z, Dirmeyer PA, Bonan G, Oleson KW, Chan E, Verseghy D, Cox P, Davies H, Kowalczyk E (2006) GLACE: the global land-atmosphere coupling experiment. Part I: overview. J Hydrometeorol 7(4):590–610

Leuning R, Van Gorsel E, Massman WJ, Isaac PR (2012) Reflections on the surface energy imbalance problem. Agric For Meteorol 156:65–74

Li Z, Tang H, Zhang B, Yang G, Xin X (2015) Evaluation and intercomparison of modis and geov1 global leaf area index products over four sites in north china. Sensors 15(3):6196–6216

Liebethal C, Huwe B, Foken T (2005) Sensitivity analysis for two ground heat flux calculation approaches. Agric For Meteorol 132(3-4):253–262

Liu H, Peters G, Foken T (2001) New equations for sonic temperature variance and buoyancy heat flux with an omnidirectional sonic anemometer. Boundary-Layer Meteorol 100(3):459–468

Mahrt L, Ek M (1984) The influence of atmospheric stability on potential evaporation. J Clim Appl Meteorol 23(2):222–234

Mauder M, Foken T (2006) Impact of post-field data processing on eddy covariance flux estimates and energy balance closure. Meteorol Z 15(6):597–609

Mauder M, Foken T (2011) Documentation and instruction manual of the eddy-covariance software package TK3 https://epub.uni-bayreuth.de/342/1/ARBERG046.pdf

Mauder M, Cuntz M, Drüe C, Graf A, Rebmann C, Schmid HP, Schmidt M, Steinbrecher R (2013) A strategy for quality and uncertainty assessment of long-term eddy-covariance measurements. Agric For Meteorol 169:122–135

Maussion F, Scherer D, Mölg T, Collier E, Curio J, Finkelnburg R (2014) Precipitation seasonality and variability over the tibetan plateau as resolved by the high asia reanalysis. J Climate 27(5):1910–1927

Meyers TP, Hollinger SE (2004) An assessment of storage terms in the surface energy balance of maize and soybean. Agric For Meteorol 125(1):105–115

Mitchell K (2005) The community noah land-surface model (lsm). User's Guide Recovered from ftp://ftp emc ncep noaa gov/mmb/gcp/ldas/noahlsm/ver_2 7

Mohan M, Bhati S (2011) Analysis of WRF model performance over subtropical region of Delhi, India. Adv Meteorol 2011:621,235

Moncrieff J, Clement R, Finnigan J, Meyers T (2004) Averaging, detrending, and filtering of eddy covariance time series. In: Handbook of micrometeorology, Springer, Berlin, pp 7–31

Moncrieff JB, Massheder J, De Bruin H, Elbers J, Friborg T, Heusinkveld B, Kabat P, Scott S, Soegaard H, Verhoef A (1997) A system to measure surface fluxes of momentum, sensible heat, water vapour and carbon dioxide. J Hydrol 188:589–611

Nakai T, Shimoyama K (2012) Ultrasonic anemometer angle of attack errors under turbulent conditions. Agric For Meteorol 162:14–26

Neftel A, Spirig C, Ammann C (2008) Application and test of a simple tool for operational footprint evaluations. Environ Pollut 152(3):644–652

Nemunaitis-Berry KL, Klein PM, Basara JB, Fedorovich E (2017) Sensitivity of predictions of the urban surface energy balance and heat island to variations of urban canopy parameters in simulations with the WRF model. J Appl Meteorol Climatol 56(3):573–595

Niemelä S, Räisänen P, Savijärvi H (2001) Comparison of surface radiative flux parameterizations: Part i: Longwave radiation. Atmos Res 58(1):1–18

Oncley SP, Foken T, Vogt R, Kohsiek W, DeBruin H, Bernhofer C, Christen A, Van Gorsel E, Grantz D, Feigenwinter C, Lehner I (2007) The energy balance experiment EBEX-2000. Part I: overview and energy balance. Boundary-Layer Meteorol 123(1):1–28

Panda J, Sharan M (2012) Influence of land-surface and turbulent parameterization schemes on regional-scale boundary layer characteristics over northern india. Atmos Res 112:89–111

Papale D, Reichstein M, Aubinet M, Canfora E, Bernhofer C, Kutsch W, Longdoz B, Rambal S, Valentini R, Vesala T, Yakir D (2006) Towards a standardized processing of net ecosystem exchange measured with eddy covariance technique: algorithms and uncertainty estimation. Biogeosciences 3(4):571–583

Patil M, Waghmare R, Halder S, Dharmaraj T (2011) Performance of noah land surface model over the tropical semi-arid conditions in western india. Atmos Res 99(1):85–96

Patil M, Kumar M, Waghmare R, Dharmaraj T, Mahanty N (2014) Evaluation of noah-lsm for soil hydrology parameters in the indian summer monsoon conditions. Theor Appl Climatol 118(1-2):47–56

Paul S, Ghosh S, Oglesby R, Pathak A, Chandrasekharan A, Ramsankaran R (2016) Weakening of indian summer monsoon rainfall due to changes in land use land cover. Scientific Reports 6

Pielke RA (2001) Influence of the spatial distribution of vegetation and soils on the prediction of cumulus convective rainfall. Rev Geophys 39(2):151–177

Pitman A (2003) The evolution of, and revolution in, land surface schemes designed for climate models. Int J Climatol 23(5):479–510

Prasad R, Sharma A, Mehrotra P (2016) Ground water year book uttar pradesh (2014 - 2015)

Radell DB, Rowe CM (2008) An observational analysis and evaluation of land surface model accuracy in the nebraska sand hills. J Hydrometeorol 9(4):601–621

Reichstein M, Falge E, Baldocchi D, Papale D, Aubinet M, Berbigier P, Bernhofer C, Buchmann N, Gilmanov T, Granier A, Grünwald T, Havránková K, Ilvesniemi H, Janous D, Knohl A, Laurila T, Lohila A, Loustau D, Matteucci G, Meyers T, Miglietta F, Ourcival J, Pumpanen J, Rambal S, Rotenberg E, Sanz M, Tenhunen J, Seufert G, Vaccari F, Vesala T, Yakir D, Valentini R (2005) On the separation of net ecosystem exchange into assimilation and ecosystem respiration: review and improved algorithm. Global Change Biology 11(9):1424–1439

Rodell M, Houser P, Jambor U, Gottschalck J, Mitchell K, Meng C, Arsenault K, Cosgrove B, Radakovich J, Bosilovich M, Entin J (2004) The global land data assimilation system. Bull Am Meteorol Soc 85(3):381

Roxy MK, Ritika K, Terray P, Murtugudde R, Ashok K, Goswami B (2015) Drying of indian subcontinent by rapid indian ocean warming and a weakening land-sea thermal gradient. Nat communications 6

Ruppert J, Thomas C, Foken T (2006) Scalar similarity for relaxed eddy accumulation methods. Boundary-Layer Meteorol 120(1):39–63

Saha A, Ghosh S, Sahana A, Rao E (2014) Failure of cmip5 climate models in simulating post-1950 decreasing trend of indian monsoon. Geophys Res Lett 41(20):7323–7330

Sahu L, Sheel V, Pandey K, Yadav R, Saxena P, Gunthe S (2015) Regional biomass burning trends in india: Analysis of satellite fire data. J Earth Syst Sci 124(7):1377–1387

Samala BK, Nagaraju C, Banerjee S, Kaginalkar A, Dalvi M (2013) Study of the indian summer monsoon using WRF–ROMS regional coupled model simulations. Atmos Sci Lett 14(1):20–27

Schotanus P, Nieuwstadt F, De Bruin H (1983) Temperature measurement with a sonic anemometer and its application to heat and moisture fluxes. Boundary-Layer Meteorol 26(1):81–93

Seneviratne SI, Stöckli R (2008) The role of land-atmosphere interactions for climate variability in europe. In: Climate Variability and Extremes during the Past 100 years, Springer, Berlin, pp 179–193

Sharma BR, Amarasinghe UA, Ambili G (2010) Tackling water and food crisis in south asia: Insights from the indo-gangetic basin

Siderius C, Hellegers P, Mishra A, van Ierland E, Kabat P (2014) Sensitivity of the agroecosystem in the ganges basin to inter-annual rainfall variability and associated changes in land use. Int J Climatol 34(10):3066–3077

Stoy PC, Mauder M, Foken T, Marcolla B, Boegh E, Ibrom A, Arain MA, Arneth A, Aurela M, Bernhofer C, Cescatti A (2013) A data-driven analysis of energy balance closure across FLUXNET research sites: The role of landscape scale heterogeneity. Agric For Meteorol 171:137–152

Suni T, Guenther A, Hansson H, Kulmala M, Andreae M, Arneth A, Artaxo P, Blyth E, Brus M, Ganzeveld L, Kabat P (2015) The significance of land-atmosphere interactions in the earth system—ileaps achievements and perspectives. Anthropocene 12:69–84

Tang J, Wang S, Niu X, Hui P, Zong P, Wang X (2016) Impact of spectral nudging on regional climate simulation over CORDEX East Asia using WRF. Clim Dyn 12:69–84

Trenberth KE, Fasullo JT, Kiehl J (2009) Earth's global energy budget. Bull Am Meteorol Soc 90(3):311–323

Turner A, Bhat G, Evans J, Marsham J, Martin G, Parker D, Taylor C, Bhattacharya B, Madan R, Mitra A, Mrudula G (2015) Interaction of convective organization and monsoon precipitation, atmosphere, surface and sea (INCOMPASS). In: EGU General Assembly Conference Abstracts, vol 17, p 3957

Turner AG, Annamalai H (2012) Climate change and the south asian summer monsoon. Nat Clim Change 2(8):587–595

Twine TE, Kustas W, Norman J, Cook D, Houser P, Meyers T, Prueger J, Starks P, Wesely M (2000) Correcting eddy-covariance flux underestimates over a grassland. Agric For Meteorolr Meteorol 103(3):279–300

Ukkola A, De Kauwe M, Pitman A, Best M, Abramowitz G, Haverd V, Decker M, Haughton N (2016) Land surface models systematically overestimate the intensity, duration and magnitude of seasonal-scale evaporative droughts. Environ Res Lett 11(10):104,012

Unnikrishnan C, Rajeevan M, Rao SVB (2017) A study on the role of land-atmosphere coupling on the south Asian monsoon climate variability using a regional climate model. Theor Appl Climatol 127:949–964

Velde R, Su Z, Ek M, Rodell M, Ma Y (2009) Influence of thermodynamic soil and vegetation parameterizations on the simulation of soil temperature states and surface fluxes by the Noah LSM over a Tibetan plateau site. Hydrol Earth Syst Sci 13(6):759–777

Venkata Ramana M, Krishnan P, Kunhikrishnan P (2004) Surface boundary-layer characteristics over a tropical inland station: seasonal features. Boundary-layer Meteorol 111(1):153–157

Vickers D, Mahrt L (1997) Quality control and flux sampling problems for tower and aircraft data. J Atmos Ocean Technol 14(3):512–526

Vishnu S, Francis P (2014) Evaluation of high-resolution wrf model simulations of surface wind over the west coast of india. Atmos Ocean Sci Lett 7(5):458–463

Waghmare R, Dharmaraj T, Patil M (2012) Noah-lsm simulation on various soil textures in tropical semi-arid regions. Soil Sci 177(11):664–673

Webb EK, Pearman GI, Leuning R (1980) Correction of flux measurements for density effects due to heat and water vapour transfer. Q J R Meteorol Soc 106(447):85–100

Wilczak JM, Oncley SP, Stage SA (2001) Sonic anemometer tilt correction algorithms. Boundary-Layer Meteorol 99(1):127–150

Wilson K, Goldstein A, Falge E, Aubinet M, Baldocchi D, Berbigier P, Bernhofer C, Ceulemans R, Dolman H, Field C, Grelle A (2002) Energy balance closure at FLUXNET sites. Agric For Meteorol 113(1):223–243

Yamashima R, Matsumoto J, Takata K, Takahashi HG (2015) Impact of historical land-use changes on the indian summer monsoon onset. Int J Climatol 35(9):2419–2430